Earth and Planetary Science Letters 610 (2023) 118117

Contents lists available at ScienceDirect

Earth and Planetary Science Letters

journal homepage: www.elsevier.com/locate/epsl

Precessional pacing of early Proterozoic redox cycles

Margriet L. Lantink [a,b,*], Wytze K. Lenstra [a], Joshua H.F.L. Davies [c,d], Rick Hennekam [e], David McB. Martin [f], Paul R.D. Mason [a], Gert-Jan Reichart [a,e], Caroline P. Slomp [a,g], Frederik J. Hilgen [a]

[a] Department of Earth Sciences, Utrecht University, 3584 CB Utrecht, the Netherlands
[b] Department of Geoscience, University of Wisconsin–Madison, Madison, WI 53706, United States
[c] Sciences de la Terre et de l'atmosphère, Université du Québec à Montréal, Montréal, QC H2X 3Y7, Canada
[d] Department of Earth Sciences, University of Geneva, CH-1205 Geneva, Switzerland
[e] Department of Ocean Systems, Royal Netherlands Institute of Sea Research (NIOZ), 1797 NZ Texel, the Netherlands
[f] Department of Mines, Industry Regulation and Safety, Geological Survey of Western Australia, Perth, WA 6004, Australia
[g] Radboud Institute of Biological and Environmental Sciences, Radboud University, 6525 AJ Nijmegen, the Netherlands

ARTICLE INFO

Article history:
Received 19 October 2022
Received in revised form 28 February 2023
Accepted 6 March 2023
Available online 29 March 2023
Editor: B. Wing

Dataset link: https://doi.org/10.25850/nioz/7b.b.bf

Keywords:
Milankovitch climate forcing
oceanic redox cycles
banded iron formations
Great Oxidation Event

ABSTRACT

Regularly alternating reduction-oxidation (redox) patterns attributed to variations in the Earth's orbit and axis (Milankovitch cycles) are widely recorded in marine sediment successions of the Phanerozoic and attest to a dynamic history of biospheric oxygen in response to astronomically forced climate change. To date, however, such astronomical redox control remains elusive for much older, Precambrian intervals of the geological record that were characterized by a globally anoxic and iron-rich ocean, i.e., prior to Earth's atmospheric oxygenation (ca. 2.4–2.2 billion years ago). Here we report a detailed cyclostratigraphic and geochemical investigation of marine-sedimentary redox cycles identified in the ca. 2.46 billion-year-old Joffre Member of the Brockman Iron Formation, NW Australia, suggesting the imprint of Earth's climatic precession cycle. Around the base and top of regularly intercalated mudrock layers, we identify sharp enrichments in redox sensitive elements (Fe, S, Ca, P) that appear to represent chemical reaction fronts formed during nonsteady state diagenesis. Using a reactive transport model, we find that the formation of characteristic double S peaks required periods of increased organic matter deposition, coupled to strongly declining Fe^{2+} concentrations in the overlying water column. This combination, in turn, implies a periodic deepening of the iron chemocline due to enhanced oxygenic photosynthesis in marine surface waters, and is interpreted as the result of precession-induced changes in monsoonal intensity that drove variations in runoff and associated nutrient delivery. Our study results point to a dynamic redox evolution of Precambrian oceanic margin environments in response to Milankovitch forcing, and offer a temporal framework to investigate linkages between biological activity and the early build-up of oxygen in Earth's ocean-atmosphere system.

1. Introduction

The redox state of the ocean-atmosphere system has experienced dramatic changes over Earth history, profoundly shaping past surface environments and the biosphere across geological timescales (Lyons et al., 2014; Reinhard and Planavsky, 2020). Regular large amplitude swings in dissolved oxygen concentrations of oceanic and marine basins are known to have occurred during various intervals of the Phanerozoic, against a backdrop of a well-oxygenated atmosphere. These redox cycles, manifested as periodic bottom- or deep-water anoxia, have been attributed to astronomical-induced climate changes that originate from quasi-periodic variations in the Earth's orbit and spin axis (Milankovitch forcing on 10^4–10^6 year scale) (Rossignol-Strick, 1983; Herbert and Fischer, 1986; Reichart et al., 1998; Mitchell et al., 2008; Meyers et al., 2012; Röhling et al., 2015). The anoxic periods are typically explained by periods of enhanced water column stratification and/or biological surface productivity, which led to increased burial of organic carbon and subsequent oxygen respiration at the seafloor. At middle to low latitudes, such processes have been generally linked to variations in monsoonal intensity – affecting hydrological, atmospheric and/or oceanic circulation and associated nutrient delivery patterns – driven by Earth's climatic precession and

* Corresponding author at: Department of Geoscience, University of Wisconsin–Madison, Madison, WI 53706, United States.
E-mail address: lantink@wisc.edu (M.L. Lantink).

https://doi.org/10.1016/j.epsl.2023.118117

orbital eccentricity cycles (Rossignol-Strick, 1983; Herbert and Fischer, 1986; Beckmann et al., 2005; Röhling et al., 2015; Reichart et al., 1998; Kutzbach et al., 2008; Bosmans et al., 2015). These two Milankovitch cycles are directly coupled, where eccentricity acts as amplitude modulator of climatic precession, the principal driver of the insolation changes.

Recently, eccentricity- (Lantink et al., 2019; de Oliveira Rodrigues et al., 2019) and precession-related cycles (Lantink et al., 2022) were detected in 2.48–2.46 billion year old (Ga) banded iron formations (BIFs) deposited in the prelude to the Great Oxidation Event (GOE) at ca. 2.4–2.2 Ga (Bekker et al., 2004; Poulton et al., 2021). BIFs are iron- and silica-rich, conspicuously layered marine sedimentary rocks that are exclusively found in the Precambrian and are indicative of anoxic and ferrous iron (Fe^{2+})-rich ocean waters (Trendall, 2002; Konhauser et al., 2017). Accordingly, these recent observations raise the intriguing question how Milankovitch forcing may have influenced redox conditions of the early Earth's BIF-forming oceans, when seawater chemistry, biology and tectonic setting were fundamentally different from the Phanerozoic (Trendall, 2002; Konhauser et al., 2017. Of particular interest in this regard is whether astronomical climate forcing might have played a (modulating) role in the early oxygenation history of the Earth, as increasing lines of geochemical evidence point to the occurrence of transient, low-level oxygen accumulation in marine shelf environments and possibly the atmosphere ('whiffs of oxygen') prior to the GOE onset (Anbar et al., 2007; Frei et al., 2009; Koehler et al., 2018). These transients in oxygenation have been estimated to occur on multi-million year timescales, while theoretical models have shown the possibility of much shorter-term, i.e., seasonal-scale oxygen variability (Lalonde and Konhauser, 2015; Reinhard et al., 2016). To date, however, the precise trajectory and pacing mechanisms of this potentially more dynamic oxygenation history remain elusive from existing geochemical archives, and the links with redox processes at the well-understood timescales of the Milankovitch cycles, which critically modulate the seasonal cycle, are currently unexplored.

In this study we aim to acquire initial insight into the influence of Milankovitch forcing on marine redox conditions of the early Earth prior to its widespread oxygenation during the GOE. We present high-resolution cyclostratigraphic and geochemical analysis of precession-scale redox cycles that we identified in the lower Paleoproterozoic Brockman Iron Formation (IF) of the Hamersley Group in NW Australia (Fig. 1). More specifically, our study focuses on the regular 'Knox cyclothem' in the Joffre Member BIF of the Brockman IF. The Knox cyclothem is a characteristic centimeter- to decimeter-scale, rhythmic lithological alternation that was first described by A. F. Trendall in the late 1960's (Trendall, 1969), and hypothesized to be linked to astronomical climate forcing (Trendall and Blockley, 1970; Trendall, 1972). In a recent study (Lantink et al., 2022), cyclostratigraphic evidence was presented for a precession origin of Knox cyclothems studied at Joffre Falls (Fig. 1a) and was independently corroborated by results of high-precision U–Pb zircon dating of a lateral drill core (DD98SGP001) (Figs. 1b and 1c). The cyclostratigraphic results from Joffre Falls were subsequently employed to determine the shorter precession period, Earth–Moon distance and length-of-day (Lantink et al., 2022). But in addition, intriguing similarities were noted between the internal build-up of the Knox cyclothems exposed at Joffre Falls and astronomical-forced redox cycles known from the Mediterranean Miocene and Pliocene (van Hoof et al., 1993; van Os et al., 1994).

This preliminary observation calls for a more detailed, chemostratigraphic investigation into the paleoenvironmental origin and significance of the cyclothems. The alternations observed in the field at Joffre Falls, however, are less suitable for this purpose due to their limited accessibility and potential effects of surface weathering. Instead, we concentrate our analysis here on core DD98SGP001, in which well-preserved strata from the Joffre Member were retrieved at ~150 km lateral distance from the Falls (Fig. 1a), and in which a similarly regular expression of unweathered cyclothems was distinguished.

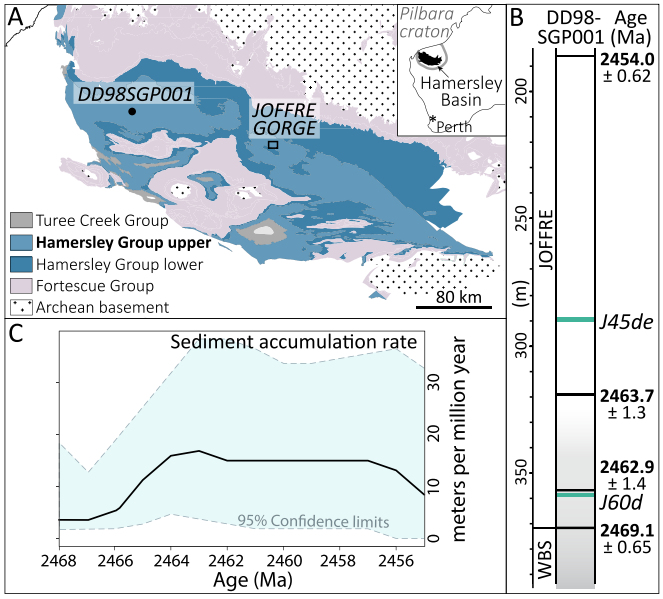

Fig. 1. Geological setting and U–Pb geochronology for the Joffre Member of the Brockman Iron Formation. (**A**) Geological map of the Hamersley Range in NW Australia showing the extent of the Brockman Iron Formation in the upper Hamersley Group and the locations of core DD98SGP001 (22°03′29.9″S 116°50′06.0″E) and section Joffre Falls in Joffre Gorge. (**B**) Schematic column of core DD98SGP001 indicating the positions of sections J45de and J60 and the $^{207}Pb/^{206}Pb$ ages of Lantink et al. (2022). Grey color gradient indicates a change from shaley carbonate-rich BIF to cherty BIF. WBS = Whaleback Shale Member. (**C**) Depositional rate model for the Joffre Member by Lantink et al. (2022) with 97.5% confidence intervals indicated.

2. Geological setting

The Joffre Member forms the second and thickest BIF unit (~350 m) of the Brockman IF within the Neoarchean to early Paleoproterozoic Hamersley Group, Hamersley Basin, which extends across the southern portion of the Pilbara Craton in northwestern Western Australia (Fig. 1 and *supplementary Fig. S1*). The iron formations of the Hamersley Group are classically interpreted as being deposited in an outer shelf environment (Trendall and Blockley, 1970; Morris and Horwitz, 1983) during sea level high-stands (Simonson and Hassler, 1996), given their frequent interstratification with organic-rich shales and carbonates that are considered shallower water equivalents (Simonson and Hassler, 1996; Klein and Beukes, 1989). However, a deeper-marine basin floor setting has been alternatively proposed (Krapež et al., 2003; Pickard et al., 2004). Absence of current- or wave-generated structures in BIF indicates deposition below storm wave base (150–200 m), but shallow enough for carbonate deposition and preservation (i.e., above the carbonate compensation depth) (Simonson and Hassler, 1996).

The BIFs of the Brockman IF, and coeval Kuruman IF in South Africa, are unparalleled in the Precambrian rock record in terms of stratigraphic thickness (i.e., multiple hundreds of meters), lateral continuity (i.e., several hundreds of kilometers) and preservation (i.e., very low metamorphic grade), rendering these deposits as valuable paleoenvironmental and, possibly, paleoclimate archives. In particular, meter- to decimeter-scale cyclicity between iron(III) oxide-rich 'BIF' and iron(II) silicate- and carbonate-rich 'shale' observed in both the Brockman and Kuruman IFs suggest Milankovitch forcing at the scale of Earth's orbital eccentricity vari-

ations (Lantink et al., 2019; de Oliveira Rodrigues et al., 2019), while decimeter- to centimeter-scale Knox cyclothem alternations in the Joffre Member were recently linked to climatic precession (Lantink et al., 2022). Paleomagnetic reconstructions (de Kock et al., 2009; Gumsley et al., 2017) and lithostratigraphic similarities between the Brockman and Kuruman IF (Trendall, 1969; Cheney, 1996; Martin et al., 1998; Beukes and Gutzmer, 2008) suggest that the two IF units may have been deposited in a single large basin or along a contiguous margin (spanning >1000 km) of the ancient Vaalbara supercraton, situated at low to equatorial latitude and in likely connection to open ocean. As such, cyclostratigraphic and geochemical investigation of the Brockman IF cyclostratigraphy offers the potential of acquiring insights into regional-scale marine redox processes in relation to (low-latitude) astronomical climate forcing acting at the global scale.

3. Materials and methods

3.1. Sample selection

Our study focused on the Joffre Member in core DD98SGP001 (diamond drill-core 1998 Silvergrass Peak #001; 22°03′29.9″S 116°50′06.0″E), which intersects well-preserved strata of the Joffre, Whaleback Shale and Dales Gorge Members of the Brockman IF from 87.7 m to 450.5 m depth (Fig. 1 and *supplementary Fig. S1*). Visual inspection of the DD98SGP001 (DD98) stratigraphy was carried out during a several-day visit to the Perth Core library of the Geological Survey of Western Australia, where the core is currently stored, after which representative intervals were selected from the lower ∼100 m of the Joffre Member that showed a particularly regular expression of the Knox cyclothem (*supplementary Fig. S2*). The two shorter core sections J45de (box 45, rows d and e) and J60d (box 60, row d) presented in this paper come from 289.05–290.26 m depth, a cherty BIF interval, and from 358.34–358.73 m depth, a shaley carbonaceous BIF interval, respectively (*supplementary Fig. S3*). The selected intervals were subsequently cut in halves to generate a flat surface along the length of the sampled core. Specific intervals were additionally polished to facilitate detailed inspection of sedimentary textures and mineralogy using high magnification scans (*supplementary Fig. S4*); the mineralogy was confirmed by thin section petrography and X-ray diffraction analysis (data not shown).

3.2. Geochemical analyses

3.2.1. XRF core scanning

X-ray fluorescence (XRF) core scanning of the selected core sections was conducted with the Avaatech core scanner at the Royal Netherlands institute of Sea Research (NIOZ), which is equipped with a new generation XRF detector yielding improved spectral resolution (Hennekam et al., 2019). The tube energy settings (1–50 kV at a maximum of 2 mA), primary beam filters and measurement time were optimized for minor/trace elements while maintaining a dead time between 20 to 40% (*supplementary Table S1*). The XRF analyses were carried out with a 12 × 1 mm slit, at 1 mm intervals, on freshly cut surfaces and covered with a 4-µm SPEX-Certi Ultralene foil to prevent cross contamination. Prior to the analyses, the cores were placed in split plastic tubes and supported from underneath with foam to create a stable and even surface. Data points associated with core breaks were removed if the total yield (sum intensities in 10 kV range) was significantly lower than that of the surroundings. Repeated analyses (n = 37) of reference sample SARM 4 in between runs indicate a precision (relative standard deviation) of <1% for Fe; <4% for Al, Ca, K, Mn; <7% for S implying that the detector remained stable during the whole experiment. Spectral data (*supplementary Fig. S5*) were interpreted using bAxil spectrum analysis software developed by Brightspec.

3.2.2. ICP-OES

Inductively coupled plasma optical emission spectrometry (ICP-OES) analysis was carried out on 14 discrete samples to convert raw XRF intensities to approximate concentrations. Thin (3–5 mm) core slices were obtained from two additional scanned intervals (J36c and J57e). The slices were chosen such that they captured a range of different chemical compositions as indicated by the XRF data and they were sawed as bedding parallel as possible, although this could not always be achieved due to the curved nature of the layers. Homogenized rock powders (crushed with either tungsten carbide or corundum) underwent total digestion using a procedure with HF-$HClO_4$-HNO_3 acid mixtures. The ICP-OES measurements were performed with a Spectro Ciros Vision ICP-OES at Utrecht University. Reference samples (ISE921 and PACS-2) and duplicate measurements (n = 4) indicate an accuracy and precision (reported here as deviation from reference value; relative standard deviation) of: Al (7%; ± 1%), Ba (−; ± 1%), Ca (11%; ± 0.5%), Fe (13%; ± 3%), K (7%; ± 2%), Mn (6%; ± 0.2%), P (4%; ± 1%) and S (3%; ± 2%) (*supplementary Table S2*).

3.2.3. XRF calibration

Comparison of XRF intensities to ICP-OES concentrations was done by visual alignment of the XRF slit positions and corresponding core slices. First, a calibration was attempted using common multivariate log-ratio calibration (Weltje et al., 2015). However, this led to inferior results (i.e., poor R^2 accuracy values in particular for Fe, and various discrepancies for the S and P records) compared to direct relation of counts versus concentrations. We suspect that this is because the XRF signal of the heavier elements comes from a slightly broader depth interval than for lighter elements (Potts et al., 1997), which in these thinly laminated sediments leads to compromised results when calibrating all elements together. Therefore, conversion to weight percentage was based on simple linear calibration (i.e., linear regressions in X-Y plots of intensity versus concentration). This yielded high R^2 values of the regression lines of the targeted elements: >80% for Al and Mn; ≥ 90% for Ca, Fe, K; and ≥ 95% for Ba, P and S (*supplementary Fig. S6*).

3.3. Time series analysis

Spectral analysis was carried out on the K (%) records of J45de and J60d sections (Figs. 2bc and 3bc and *supplementary Fig. S7*), which were detrended and linearly interpolated at 10 mm and 1 mm, respectively. In addition, normalized ferric oxide abundance records of two longer core intervals were selected for the analysis of longer-period cycles (Figs. 2a and 3a). These ferric oxide records are based on mineral reflectance data acquired by the Hyperspectral scanner of the Geological Survey of Western Australia (Hancock et al., 2013) and were extracted from The Spectral Geologist spectral interpretation software at a resolution of 1 cm. We used multitaper method (MTM) spectral analysis (Thomson, 1982) as implemented in the R package astrochron (Meyers, 2014) using three 2π slepian tapers and a time-bandwidth product of 3. Classical AR1 and LOWSPEC (Meyers, 2012) confidence levels were determined using the functions 'mtm' and 'lowspec'. Astrochron was further used for rectangular bandpass filtering ('bandpass').

3.4. Reactive transport modeling

3.4.1. Model setup

A reactive transport model (RTM) was used to investigate the formation of the characteristic Fe and S enrichments associated with the studied Knox cyclothems (Figs. 2c and 3c and *supplementary Fig. S7*). The model describes the mass balance of 6 dissolved and 7 particulate species (*supplementary Table S3*) and is a modified version of that of Lenstra et al. (2018) based on Wang

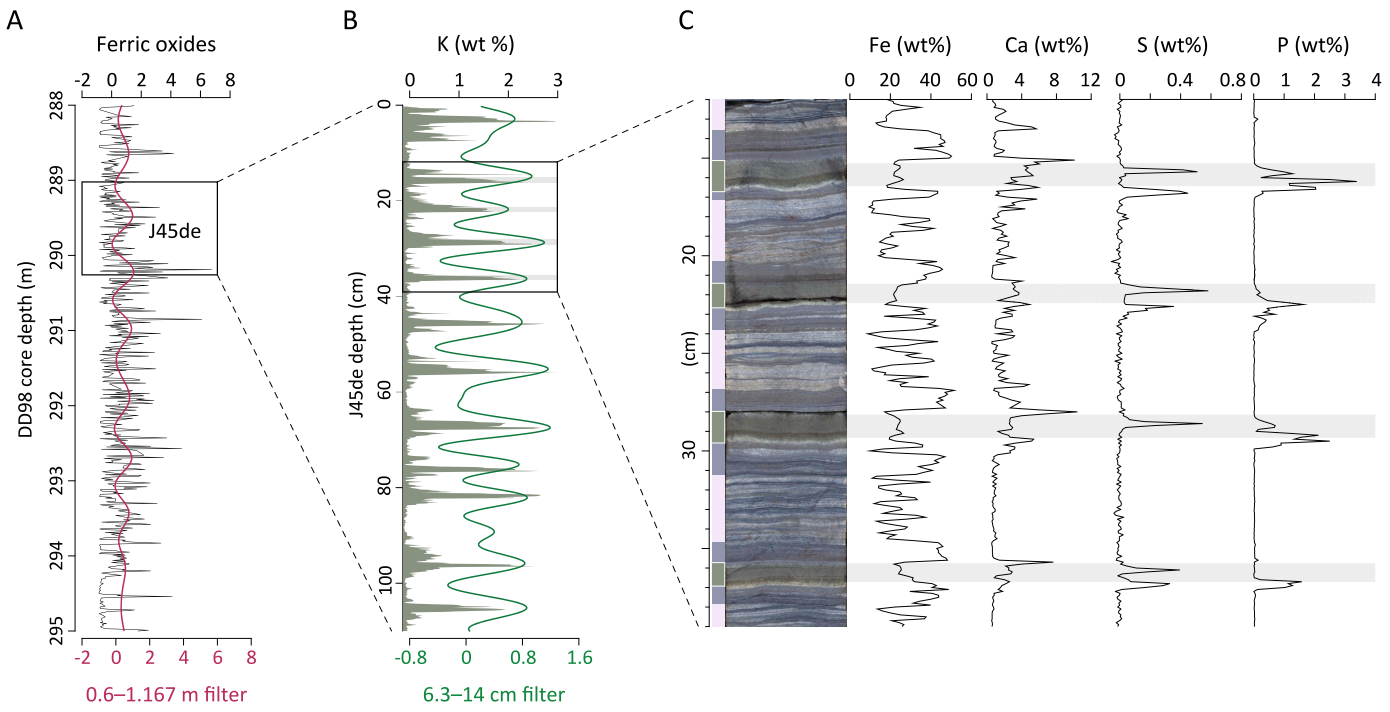

Fig. 2. Cyclostratigraphy and high-resolution geochemistry of selected interval J45de in core DD98. (**A**) Normalized ferric oxide abundance record (thin black line) of a larger stratigraphic interval encompassing section J45de, showing the expression of both the regular small-scale (Knox cyclothem) alternations and larger-scale cyclicity as highlighted by the bandpass filtered signal (thick red line). (**B**) Regular small-scale alternations reflected in the K weight % record of section J45de and corresponding bandpass filtered curve (thick green line). (**C**) Detail of four Knox cyclothem alternations from section J45de showing the lithology on the left and the Fe, Ca, S and P wt% records on the right. Grey horizontal bands mark the position of the peaks in K wt% as visible in the inset in (B). Vertical bars to the left of the core: green = stilpnomelane-carbonate mudrock layers; dark blue-purple = iron oxide-dominated zones; light beige = microbanded chert intervals.

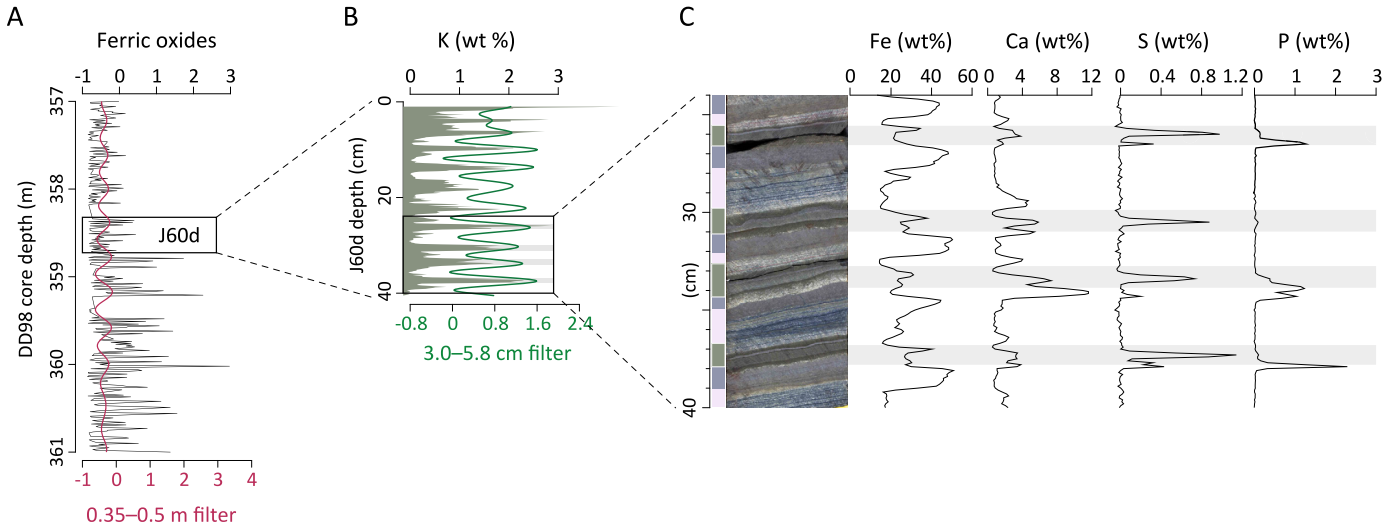

Fig. 3. Cyclostratigraphy and high-resolution geochemistry of selected interval J60d in core DD98. (**A**) Normalized ferric oxide abundance record (thin black line) of a larger stratigraphic interval encompassing section J60d, showing the expression of both the regular small-scale (Knox cyclothem) alternations and larger-scale cyclicity as highlighted by the bandpass filtered signal (thick red line). (**B**) Regular small-scale alternations reflected in the K weight % record of section J60d and corresponding bandpass filtered curve (thick green line). (**C**) Detail of four Knox cyclothem alternations from section J60d showing the lithology on the left and the Fe, Ca, S and P wt% records on the right. Grey horizontal bands mark the position of the peaks in K wt% as visible in the inset in (B). Vertical bars to the left of the core: green = stilpnomelane-carbonate mudrock layers; dark blue-purple = iron oxide-dominated zones; light beige = microbanded chert intervals.

and Van Cappellen (1996) extended here to include the formation of magnetite (Fe_3O_4). A detailed description of the model and model settings is given in the *supplementary Methods S1* and *Tables S3–8*.

In the RTM, we based the sedimentation rate on the U–Pb results of Lantink et al. (2022), which indicate an average compacted rate of ca. 1 cm/kyr (Fig. 1c), consistent with a precession origin (11 kyr) for the ~10 cm thick Knox cyclothems. Assuming a porosity of 0.95, the sedimentation rate at the sediment-water interface in the model is 0.02 cm yr^{-1} (*supplementary Table S8*). Bottom water concentrations of solutes are based on literature while fluxes of solids towards the sediment-water interface are constrained by the XRF records (*supplementary Table S8*). Prior to our transient scenarios, the model was run to steady state for 17.000 years with the boundary conditions at the sediment-water interface as given in *supplementary Table S8*.

3.4.2. Transient model scenarios

In our first transient scenario, we tested whether the characteristic Fe and S profiles, determined by XRF core scanning (Figs. 2c and 3c and *supplementary Fig. S8*), could be reproduced by only varying the input of organic matter. In this scenario a constant flux of Fe oxides to the sediment water interface and constant bottom water Fe^{2+} was assumed (*supplementary Table S8*). The organic matter flux was increased to 4.3 µmol cm^{-2} yr^{-1} for a period of 4 kyr (*supplementary Fig. S9*) to simulate the deposition of the green mudrock layers of the Knox cyclothems. In this scenario, the total organic carbon content at the sediment water interface increased from ca. 0.03 to 1.8 wt%.

Since the characteristic double S enrichments could not be reproduced with this initial scenario (see Section 4.3), we applied a second transient scenario that included the same temporal trend in organic matter input (*supplementary Fig. S11*), but we now also prescribed a decrease in the Fe oxides input, which we set at ca. 1% of the baseline scenario. In addition, the bottom water Fe^{2+} concentrations during this period were decreased to 0 µmol L^{-1} (*supplementary Fig. S11*). A more detailed description of the different model scenarios can be found in Section 4.3 and *supplementary Methods S2*.

4. Results and discussion

4.1. Knox cyclothems in core DD98 and cyclostratigraphic interpretation

During visual inspection of the DD98 core stratigraphy, we encountered a particularly prominent, regular and continuous expression of Knox cyclothems in the lower ~100 m of the Joffre Member. In this part of the core, the basic structure of the Knox cyclothem is defined by a 1) greenish-brown, carbonaceous mudrock layer (~0.5–1 cm thick) with a 2) microbanded iron oxide-rich band above and/or below, alternating with 3) microbanded chert. Note, however, that a wide variety in specific lithological expression of cyclothems can be distinguished (*supplementary Fig. S2*). The thickness of the alternations typically ranges between 5 and 15 cm. The alternations in selected core section J45de, which are representative of cherty iron formation-type cyclothems, are generally two to three times thicker than the shaley carbonate-type cyclothems, as in selected core section J60d, which contain thinner cherts and lack a second iron oxide-rich band on top of the mudrock layers (*supplementary Results*).

To independently test our climatic precession hypothesis for the Knox cyclothems in the core, we first conducted a cyclostratigraphic study focusing on selected geochemical records. In search for cyclicity, the elemental records of K (%) and the detrital elements (Al, Rb, Ti, Zr), obtained by calibrated XRF core scanning (Section 4.2), proved to be most suitable: the records show repeated, well-defined maxima at the position of the greenish mudrock layers, emphasizing the regular character of the cyclothems (Figs. 2b and 3b and *supplementary Fig. S7*). In addition, two longer records of abundance variations in ferric oxide minerals were analyzed; these records, which encompass the J45de and J60d segments of the core, are available from hyperspectral core scanning (Section 4.3) and reveal a clear amplitude modulation of the basic cyclothem alternations (Figs. 2a and 3a). Consistent with the visual observations, multitaper method (MTM) spectral analysis of the K % records indicates dominant cyclicity around 7–13 cm and ~4.5 cm for the studied J45de and J60d intervals, respectively, with spectral peaks exceeding 95–99% confidence limits (Fig. 4a). In addition, the MTM power spectra of the two longer ferric oxide records provide indications for the presence of a larger-scale modulating cycle with thicknesses of 88 cm and 41 cm in the intervals that include J45de and J60d, respectively (Fig. 4b). Thus, a

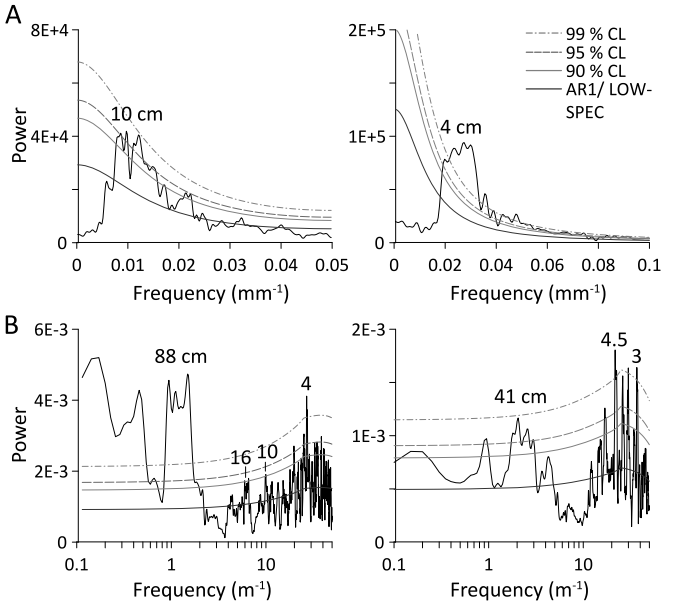

Fig. 4. Power spectral analysis. (**A**) MTM spectra for the K wt % records of J45de (*left*) and J60d (*right*) with autoregressive noise (AR1), 90, 95 and 99% confidence levels (CL). Spectral peak labels (in cm) correspond to the mean periodicity of the small-scale cyclicity (Knox cyclothems) in these two intervals. (**B**) MTM spectra for the ferric oxide abundance records of J45de (*left*) and J60d (*right*) with LOWSPEC background estimation, 90, 95 and 99% confidence levels. The peaks at 88 cm (J45de) and 41 cm (J60d) represent significant f-test peaks that correspond to the larger-scale cyclicity as seen in Figs. 2a and 3a. The peaks at 10–16 cm (J45de) and 3–4.5 cm (J60d) are related to the small-scale (Knox cyclothem) cyclicity. The strong peak around 4 cm in the MTM spectrum of J45de results from the occurrence of double ferric oxide maxima per single small-scale cycle (Fig. 2a), which is related to the quadripartite structure of the Knox cyclothems (i.e., chert – iron oxide – mudrock – iron oxide; Fig. 2c).

~1:9 thickness ratio is observed between the cyclothems and the longer-period modulating cycle in both these records.

The cyclostratigraphic results from core DD98 turn out to be in agreement with the earlier cyclostratigraphic observations from Joffre Falls, where on average nine Knox cyclothems with an average thickness of approximately 9 cm are bundled into ~85 cm thick alternations of 'BIF' and more weathering prone 'shale' (Lantink et al., 2022). This cycle hierarchy has been related to the combined influence of climatic precession and short (~100 kyr) eccentricity, taking into account that a shorter precession period is expected due to a reduced Earth–Moon distance in the distant past (Berger and Loutre, 1994; Waltham, 2015); this precession period was estimated to be ~11 kyr at ca. 2.46 Ga (Lantink et al., 2022). In addition, recently established high-precision U–Pb ages from DD98 (Lantink et al., 2022) (Fig. 1b) suggest that the average sedimentation rate in the DD98 core increased from 4 m/Myr in the lowermost part of the Joffre Member to 15 m/Myr higher up in the core (Fig. 1c). This estimated rate is within error consistent with a ~11 kyr duration for both the ~9 cm-thick Knox cyclothems in section J45de and the ~4 cm-thick cyclothems in section J60d, considering that the J60d cyclothems originate from the lowermost part of the Joffre Member where sedimentation rates were reduced.

Hence, the consistency between the cyclostratigraphic results of Joffre Falls (Lantink et al., 2022) and core DD98 on the one hand, and on the other hand the U–Pb geochronology of Lantink et al. (2022), provides mutually supportive evidence for the interpretation that the Knox cyclothems in the Joffre Member – observed in both the field and in the core – are probably related to climatic precession. As such, we now shift our attention to the specific lithological and geochemical characteristics of the cyclothems in the core which may inform us about potential astronomical con-

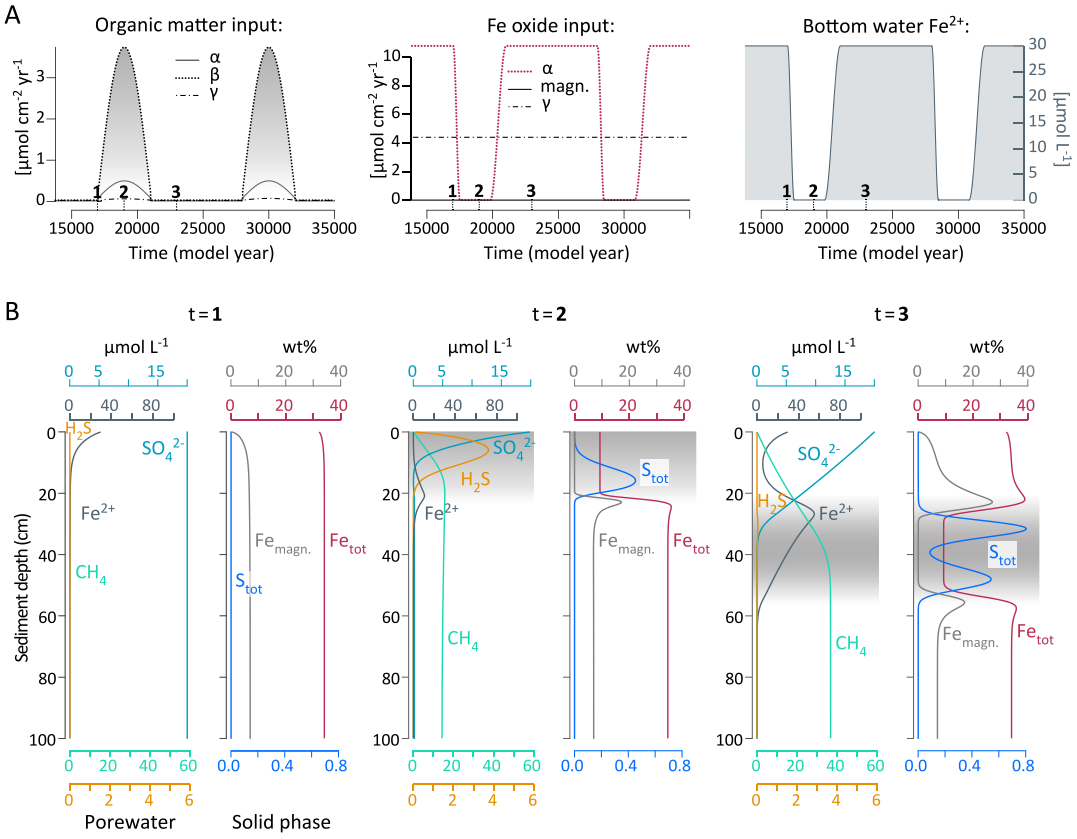

Fig. 5. Model scenario with variable organic matter and iron input. Results of the RTM demonstrating the formation of diagenetic magnetite and pyrite laminae (two Fe and S maxima). (**A**) Transient scenario for the input of organic matter and Fe oxides to the sediment-water interface and bottom water Fe^{2+} for two successive precession cycles. The different types of organic matter are denoted as α (highly reactive), β (less reactive) and γ (refractory); different types of Fe oxides as α (highly reactive), magnetite and γ (refractory). 1, 2 and 3 indicate the time points shown in (B). Note that the width of the OM peak is larger than that of the Fe oxide and bottom water Fe^{2+} minimum. (**B**) Modeled porewater (Fe^{2+}, SO_4^{2-}, H_2S and CH_4) and solid phase depth profiles (total Fe oxides, magnetite and total S) for three time points indicated in (A): before (t = 1), during (t = 2) and after (t = 3) deposition of the organic matter-rich layer. The grey shaded zones indicate the depth interval of enhanced organic matter deposition.

trols on the redox dynamics of the environment during their deposition.

4.2. Patterns indicative of early diagenetic redox changes

When zooming-in on the individual Knox cyclothems, a systematic pattern of distinctive, sharply defined laminae of redox-sensitive minerals and corresponding element enrichments is revealed by our analysis of sections J45de and J60d (Figs. 2c and 3c and *supplementary Fig. S7*). At or close to the bottom and top of the regular mudrock layers, we note the presence of thin, conspicuous laminae of magnetite and pyrite, which are visible as sharp and often double peaks in Fe and S, respectively, in the XRF data. The Fe and S enrichments have a symmetrical arrangement, whereby pyrite laminae (S peaks) are always located on the inner side of magnetite laminae (Fe peaks) and/or the iron oxide-rich bands (Fe plateaus) that precede or surround the mudrock layers. In addition, distinct laminae of beige-white carbonate (Ca) and phosphorus (P) enrichments are observed.

The pronounced enrichments of redox-sensitive minerals/elements in discrete, sometimes wavy ('fluid-like') horizons that show a cross-cutting relationship with the normal bedding (*supplementary Figs. S2, S4 and S8*), is incompatible with a purely 'primary' sedimentary origin. Rather, these features are strongly reminiscent of in-situ chemical redistribution and reaction processes arising from the breakdown of organic matter (OM) during early diagenesis (Berner, 1981; Kasten et al., 2003). Such authigenic mineral laminae, which can be preserved on geological time scales, point towards nonsteady-state diagenesis (Berner, 1969; de Lange et al., 1987; van Hoof et al., 1993; Passier et al., 1996; Kasten et al., 2003). Non-steady state conditions typically occur where strong gradients existed in the net OM content (relative to available oxidants) of the sediment. In the case of the Knox cyclothems, the symmetrical arrangement of the double S and Fe horizons around the mudrock layers points to a marked increase in the net arrival of organic matter at the seafloor during the mudrock phase of the precession cycle, as further detailed below.

The systematic positioning of the double pyrite laminae (S peaks) on the inner side of the iron oxide bands and/or magnetite laminae (Fe plateaus and peaks, respectively) suggest a specific nonsteady-state situation (Berner, 1969) involving the development of sulfide (H_2S) in the mudrock porewaters, as a consequence of organic matter oxidation with SO_4^{2-}. Similar iron sulfide and -oxide enrichment patterns have been described for Pliocene-Pleistocene sapropel alternations, where they reflect the formation of 'redox fronts' involving diffusion of H_2S, Fe^{2+} and O_2 during burial (van Hoof et al., 1993; Passier et al., 1996). During the early Paleoproterozoic, however, seawater SO_4^{2-} concentrations have been estimated to be three orders of magnitude lower and iron (hydr)oxides, precipitated from the photic zone, are considered the dominant primary oxidants for organic matter on the seabed during BIF formation (Konhauser et al., 2017). Thus, understanding how the observed Fe and S patterns can be generated and translated to precession-induced processes in the early Paleoproterozoic water column, requires a further examination of the early diagenetic processes itself. For this purpose, a reactive transport model (RTM) (Lenstra et al., 2018) was employed, which provides

a quantitative framework to study the biogeochemical redox reactions taking place below the sediment-water interface.

4.3. Simulating the Fe and S patterns with a reactive transport model

We specifically applied the RTM to investigate whether variations in the flux of organic matter (OM) versus iron (hydr)oxides (FeOx) and bottom water Fe^{2+} concentrations allow a quantitative reconstruction of the characteristic Fe and S profiles on the timescale of precession (Section 4.4). In the model, we assumed a permanently anoxic water column with a bottom water SO_4^{2-} concentration of 20 µmol L^{-1} (*supplementary Tables S3–8*). The Fe in the iron oxide-rich beds was modeled by assuming a constant high FeOx flux of 0.11 mol m^{-2} yr^{-1}. We are primarily interested in the transitions from low to high OM flux, hence the processes driving the formation of iron-poor chert layers are not included in the model scenario. The deposition of the mudrock layers was simulated by imposing an increase in the OM flux from zero to 0.04 mol m^{-2} yr^{-1} (1.8 weight % organic C) for a period of 4 kyr (about $1/3^{rd}$ of the precession cycle). The patterns that we specifically targeted were i) the magnetite laminae, represented by subtle Fe enrichments at lower and upper transitions from iron oxide to mudrock layers as observed in J45de (Fig. 2c), and ii) the pyrite laminae, visible as double S peaks on the inside.

The outcome of our data-model comparison demonstrates that, in addition to an increase in OM, a strong decline in FeOx input and porewater Fe^{2+} during deposition of the OM-rich mudrock layer is a prerequisite for the accurate reproduction of the observed S and Fe records (Fig. 5 and *supplementary Figs. S9–12*). More specifically, our model calculations imply that a strong decline in Fe oxide deposition (i.e., <1% of its original flux) and bottom water Fe^{2+} concentrations close to zero during the OM-rich phase, are essential for the build-up of porewater H_2S that subsequently leads to the formation of the double S peaks (*supplementary Methods S2*). In the model, the S peaks arise from precipitation of iron sulfides (FeS_x) at two separate reaction fronts, involving H_2S and Fe^{2+}, in the basal and upper part of the OM-rich sediment interval. In addition, two narrow Fe peaks in the form of magnetite are developed around the FeS_x laminae due to the reaction of FeOx with Fe^{2+} liberated from FeOx reduction in the sediment immediately above or below the sulfidic zone in the sediment.

The double S peaks are not replicated when we prescribe a more moderate decline or continuous high FeOx flux over the modeled Knox cyclothem (*supplementary Methods S2*). Without a decline in bottom water Fe^{2+} and Fe oxide deposition, the low amounts of H_2S that are produced in the OM-rich depth interval are, once Fe oxides become depleted, directly precipitated as FeS_x due to the large availability of Fe^{2+}. As a result, only a single broad horizon of FeS_x is formed in the middle of the OM-rich depth interval (*supplementary Fig. S10*), contrary to the observed narrow, often double S peaks and their more outward position closer to the base and top of the Fe minimum (Figs. 2c and 3c and *supplementary Fig. S8*). Fundamentally, these characteristic patterns can only be explained when H_2S produced in the OM-rich layer diffuses upwards and downwards to meet Fe^{2+} liberated from FeOx reduction in the surrounding sediment (*supplementary Discussion S1*). A model sensitivity test shows that with slightly elevated bottom water Fe^{2+} concentrations (i.e., at 2.5 and 5 µmol L^{-1}), double FeS_x enrichments are still formed, but are less well resolved due to additional FeS_x precipitation in the middle of the OM-rich layer (*supplementary Fig. S13*). Higher bottom water SO_4^{2-} concentrations in the RTM (i.e., ≫20 µmol L^{-1}) yield total S concentrations that are much higher than measured S concentrations (*supplementary Table S8*). Hence, variations in seawater SO_4^{2-} over the course of the precession cycle would not explain the observed early diagenetic features. This implies that during deposition of the OM-rich mudrock layer the flux of FeOx and porewater Fe^{2+} must have been very low.

4.4. Variations in oxygenic photosynthesis and iron chemocline position related to runoff

The results of the early diagenetic modeling imply that, over the precession cycle, substantial changes occurred in the redox conditions of the seawater, resulting from changes in primary productivity. The combination of low bottom water Fe^{2+} concentrations and limited FeOx flux, required to model the distinctive Fe and S records, indicates that the water column periodically became low in dissolved Fe^{2+}. This in turn suggests that large-amplitude oscillations occurred in the vertical and lateral position of the Fe^{2+}-poor to Fe^{2+}-rich gradient or redox boundary (iron chemocline), assuming this chemocline was originally positioned within the photic zone of more proximal shelf waters (Kendall et al., 2010; Poulton and Canfield, 2011; Lyons et al., 2014; Ostrander et al., 2019). Such periodic downward shifts, reflecting a net increase in Fe^{2+} oxidation (removal) versus Fe^{2+} supply, must have resulted either directly or indirectly from increased O_2 production via oxygenic photosynthesis, given the simultaneous increase in the flux of OM inferred here. While increased photoferrotrophy likely contributed to the initial lowering of the iron chemocline, a further deepening beyond the photic limit, and the strong decoupling between OM and Fe input (increase vs. decline, respectively), can only be logically explained by enhanced cyanobacterial growth and associated OM export.

Additional lithological clues supporting the inferred shifts in chemocline position include 1) the systematic occurrence of iron oxide-rich bands immediately below the mudrock layers. These iron oxide-rich zones may be the direct result of the net Fe^{2+} oxidation and 'raining out' of iron (hydr)oxides when the iron chemocline moved downward as a consequence of increased O_2 production in shallower waters. Furthermore, 2) the systematic arrangement of sharp, double Ca peaks in the cyclothems of J45de, either just below or above the S peaks (Fig. 2c and *supplementary Fig. S7*), is compatible with preferential carbonate precipitation just outside the sulfidic zone, where higher alkalinity production and carbonate saturation is expected in association with iron reduction (Coleman, 1993; Middelburg et al., 2020). In turn, the relatively high Ca concentrations associated with these diagenetic carbonate laminae could point to enhanced precipitation of Ca^{2+}-rich carbonate when less dissolved Fe^{2+} was available (Sumner and Grotzinger, 1996). It is important to emphasize that the very low bottom-water Fe^{2+} concentrations that we invoke for the formation of the double S peaks, likely represent an end-member scenario (*supplementary Discussion S1*). We imagine that, in reality, the chemocline was dynamic also on sub-Milankovitch timescales (e.g., associated with winter mixing), and this could for example explain why the mudrock intervals still contain a considerable amount of Fe (∼20 wt%) (Figs. 2c and 3c) present in the carbonate and aluminosilicate fractions (*supplementary Discussion S1*).

The distinct P enrichment patterns (Figs. 2c and 3c) provide a potential key to understand how the variations in O_2 production and chemocline oscillations may have been brought about by precessional forcing. Their high concentrations (1–3 weight %) cannot be explained only by input of OM (organic P < 0.01%), given a C:P ratio of the OM of 106:1 (Redfield ratio). This suggests an additional major input of phosphate originating directly or indirectly from the water column (*supplementary Discussion S1*). The significantly higher proportion of aluminosilicate clay in the mudrock layers (*supplementary Fig. S7*), indicating enhanced terrigenous input, suggests that the phosphate source may also have been terrestrial, and was periodically introduced via distal continental

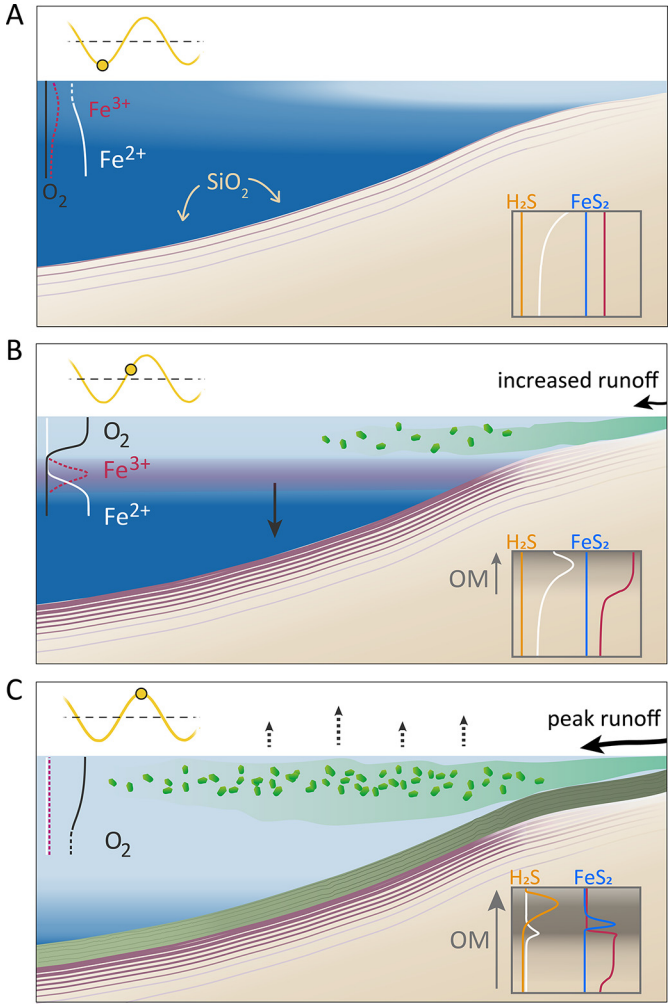

Fig. 6. Conceptual climate model for redox oscillations during the early Paleoproterozoic. (**A**–**C**) show the progression from summer insolation minimum to maximum (position on yellow curve in the upper left) and the proposed monsoonal response. Middle left of each panel: interpreted water column redox structure. Bottom right inset: sedimentary redox profile (RTM summary – schematic of Fig. 5). Dark grey colors denote organic matter, green = cyanobacteria (water column) and terrigenous material (sediment floor), red purple = iron oxide, beige = chert. Black arrow in (**B**) indicates downward movement of the iron chemocline, causing enhanced 'rain down' of iron (hydr)oxides. Dotted arrows in (**C**) denote possible net O_2 diffusion to the atmosphere during periods of maximum water column oxygenation.

runoff during precession-induced wetter climatic conditions. As P is commonly considered the ultimate limiting nutrient for oxygenic photosynthesis on geological timescales (Tyrrel, 1999) such periodic enhanced riverine input of P could have acted as a critical primary productivity stimulant (Bjerrum and Canfield, 2002; Jones et al., 2015).

4.5. Conceptual Milankovitch forcing model for early Proterozoic BIFs and regional climate

Synthesizing our results with knowledge from the Phanerozoic, a conceptual model for precession forcing of the Knox cyclothem and regional climate system can be formulated (Fig. 6). In this conceptual model, we link the inferred variations in continental nutrient input, marine primary productivity and iron chemocline oscillations to precession-driven changes in (summer) monsoon intensity. Because monsoonal systems are highly sensitive to variations in summer insolation and seasonality, which is dominated by precession especially at low latitudes (Kutzbach et al., 2008; Bosmans et al., 2015), we consider a monsoonal control the most logical scenario given the evidence for a precession origin of the Knox cyclothems (as opposed to obliquity), and the low paleolatitude position of the Hamersley-Transvaal basin indicated by paleomagnetic reconstructions (de Kock et al., 2009; Gumsley et al., 2017). Moreover, monsoonal activity would have been intensified with the emergence of relatively large, elevated landmasses around the Archean-Proterozoic transition (Gumsley et al., 2017; Bindeman et al., 2018).

We envisage that deposition of the chert layers of the Knox cyclothems occurred when runoff and surface water oxygenation were limited, during overall dry climatic conditions at times of reduced seasonality, i.e., precession minima for the southern hemisphere or precession maxima for the northern hemisphere (Fig. 6a and *supplementary Discussion S2*). Moving toward the opposite phase of the precession cycle, the intensification of monsoonal precipitation and associated riverine nutrient input stimulated marine productivity and led to chemocline lowering and deposition of the iron oxide bands (Fig. 6b). Maximum oxygenated conditions, lowest chemocline position and organic matter burial occurred during the peak 'wet' phase at times of maximum seasonal contrast and are represented by the green mudrock layers (Fig. 6c). Our monsoonal hypothesis also applies to the meter-scale eccentricity-related alternations characteristic of the Dales Gorge Member and Kuruman IFs (Lantink et al., 2019; de Oliveira Rodrigues et al., 2019). The dominant expression of eccentricity in these IF units points to a strong non-linear response to the initial precession-induced insolation forcing.

Our study of precession-scale redox cyclicity in the Joffre Member BIF reveals a dynamic redox structure of the Neoarchean to early Paleoproterozoic continental margins, where previously geochemical reconstructions recognizing variability on the Milankovitch scale were lacking (Poulton and Canfield, 2011; Lyons et al., 2014; Kendall et al., 2010; Haugaard et al., 2016; Ostrander et al., 2019). In addition, the inferred eccentricity origin of the meter-scale variations between 'BIF' and 'shale' implies that also these facies variations are associated with laterally synchronous, widespread changes in water column biogeochemistry. This interpretation presents a significant modification to the more classical models for IF deposition, in which such stratigraphic facies changes are related, at first order, to sea level-controlled changes in proximity to the (less ferruginous and more productive) shoreline and marine surface (e.g. Beukes and Gutzmer, 2008; Konhauser et al., 2017), implying a stable chemocline position. The vertical amplitude of the proposed iron chemocline oscillations is difficult to estimate given the large uncertainty in the absolute depth of deposition and paleo-bathymetry of the Brockman IF (Morris and Horwitz, 1983; Pickard et al., 2004) (Section 3). However, we suspect that the oscillations spanned at least several tens of meters given the downward shifts from well above to below the photic limit or even the sediment-water interface, based on the Joffre Member sequences studied here.

The link with low-latitude astronomical forcing through precession and eccentricity also makes it unlikely that the redox cycles studied in core DD98 record a secondary or local phenomenon only, or conversely, represent a predominantly turbiditic signal resulting from (glacio-)eustatic sea level change (Pickard et al., 2004). Rather, the redox variations likely applied to the entire Hamersley-Transvaal region and have already been identified at Joffre Falls (Lantink et al., 2022) ~150 km to the east (Fig. 1a). Since Milankovitch forcing ultimately operates on the global scale, the alternations may be representative of other marine environments worldwide situated within the same mid- to low latitude climatic zone and in the vicinity of a large hinterland.

5. Conclusions and implications

We tentatively conclude that, as during the Phanerozoic, the redox balance of the pre-oxygenated Earth's oceanic margins was critically unstable with regards to astronomically forced insolation variations and their associated climatic and productivity response. However, where periods of higher export productivity during the Phanerozoic effectively resulted in the periodic development of deep-water ocean anoxia, precession stimulation of photosynthesis during the early Paleoproterozoic led to periodic net removal of reducing Fe^{2+}, facilitating the possible accumulation of oxygen in the shallowest ocean. In this respect, the mudrock layers of the Knox cyclothem would represent a high-frequency subtle version of the 'whiffs of oxygen' (Anbar et al., 2007; Koehler et al., 2018), with a much more regular, i.e., orbitally synchronized, occurrence. Further research should explore whether these transient oxygenation signals have a tectonic or internal feedback origin as suggested earlier (Lyons et al., 2014; Alcott et al., 2019; van de Velde et al., 2020), or whether they might alternatively be the manifestation of very long-period eccentricity maxima (Boulila et al., 2012), given their coincidence with prominent black (i.e., organic carbon- and pyrite-rich) shale intervals.

The precession-paced changes in iron and carbon drawdown in association with O_2 production may have important implications for how the early Earth's atmosphere became oxygenated. When considering the oscillations as superimposed on a gradually increasing trend, possibly related to the emergence of large landmasses and associated monsoonal intensification, we speculate that cyclically enhanced primary productivity in low-Fe^{2+} surface waters resulted in an earlier surpassing of the critical threshold for O_2 diffusion and build-up into the atmosphere (Fig. 6c), than currently known (Wogan et al., 2022). This certainly is conceivable given the timing of our targeted interval from the Joffre (ca. 2.47–2.45 Ga) with respect to the first reported evidence for atmospheric O_2 levels higher than 10^{-5} of their present value at ca. 2.43 Ga (Warke et al., 2020) marking the onset of the GOE (Poulton et al., 2021).

CRediT authorship contribution statement

Margriet L. Lantink: Conceptualization, Formal analysis, Investigation, Methodology, Project administration, Visualization, Writing – original draft, Writing – review & editing. **Wytze K. Lenstra:** Conceptualization, Methodology, Visualization, Writing – original draft, Writing – review & editing. **Joshua H.F.L. Davies:** Conceptualization, Investigation, Visualization, Writing – review & editing. **Rick Hennekam:** Investigation, Resources, Writing – review & editing. **David McB. Martin:** Resources, Writing – review & editing. **Paul R.D. Mason:** Conceptualization, Supervision, Writing – review & editing. **Gert-Jan Reichart:** Conceptualization, Resources, Supervision, Writing – review & editing. **Caroline P. Slomp:** Conceptualization, Funding acquisition, Supervision, Writing – review & editing. **Frederik J. Hilgen:** Conceptualization, Funding acquisition, Methodology, Project administration, Supervision, Visualization, Writing – review & editing.

Declaration of competing interest

The authors declare that they have no known competing financial interests or personal relationships that could have appeared to influence the work reported in this paper.

Data availability

All study data are included in the article and/or supporting information. Raw XRF core scanning data are available at NIOZ Dataverse: https://doi.org/10.25850/nioz/7b.b.bf.

Acknowledgements

We acknowledge the Geological Survey of Western Australia for providing field logistical support and core material and we thank L. Hancock and M. Wawryck for the Hylogger mineral extractions. This work was supported by the Netherlands Organisation for Scientific Research [NWO; grant number ALWOP.190]; the Netherlands Earth System Science Centre [NESSC; Gravitation-grant number 024.002.001]; and the Foundation Stichting Dr. Schürmannfonds [grant numbers 2018-136 and 2019-145].

Appendix A. Supplementary material

Supplementary material related to this article can be found online at https://doi.org/10.1016/j.epsl.2023.118117.

References

Alcott, L.J., Mills, B.J., Poulton, S.W., 2019. Stepwise Earth oxygenation is an inherent property of global biogeochemical cycling. Science 366 (6471), 1333–1337.
Anbar, A.D., Duan, Y., Lyons, T.W., Arnold, G.L., Kendall, B., Garvin, J., Buick, R., 2007. A whiff of oxygen before the great oxidation event? Science 317 (5846), 1903–1906.
Beckmann, B., Flögel, S., Hofmann, P., Schulz, M., Wagner, T., 2005. Orbital forcing of Cretaceous river discharge in tropical Africa and ocean response. Nature 437 (7056), 241–244.
Bekker, A., Holland, H.D., Wang, P.L., Rumble, D.I.I.I., Stein, H.J., Hannah, J.L., Beukes, N.J., 2004. Dating the rise of atmospheric oxygen. Nature 427 (6970), 117–120.
Berger, A., Loutre, M.F., 1994. Astronomical forcing through geological time. In: De-Boer, P.L., Smith, D.G. (Eds.), Orbital Forcing and Cyclic Sequences. International Association of Sedimentologists Special Publication, 19, pp. 15–24.
Berner, R.A., 1969. Migration of iron and sulfur within anaerobic sediments during early diagenesis. Am. J. Sci. 267 (1), 19–42.
Berner, R.A., 1981. A new geochemical classification of sedimentary environments. J. Sediment. Res. 51 (2), 359–365.
Beukes, N.J., Gutzmer, J.E.N.S., 2008. Origin and paleoenvironmental significance of major iron formations at the Archean-Paleoproterozoic boundary. Rev. Econ. Geol. 15, 5–47.
Bindeman, I.N., Zakharov, D.O., Palandri, J., Greber, N.D., Dauphas, N., Retallack, G.J., Bekker, A., 2018. Rapid emergence of subaerial landmasses and onset of a modern hydrologic cycle 2.5 billion years ago. Nature 557 (7706), 545–548.
Bjerrum, C.J., Canfield, D.E., 2002. Ocean productivity before about 1.9 Gyr ago limited by phosphorus adsorption onto iron oxides. Nature 417 (6885), 159–162.
Bosmans, J.H.C., Drijfhout, S.S., Tuenter, E., Hilgen, F.J., Lourens, L.J., 2015. Response of the North African summer monsoon to precession and obliquity forcings in the EC-Earth GCM. Clim. Dyn. 44 (1–2), 279–297.
Boulila, S., Galbrun, B., Laskar, J., Pälike, H., 2012. A ~9 myr cycle in Cenozoic δ13C record and long-term orbital eccentricity modulation: is there a link? Earth Planet. Sci. Lett. 317, 273–281.
Cheney, E.S., 1996. Sequence stratigraphy and plate tectonic significance of the Transvaal succession of southern Africa and its equivalent in Western Australia. Precambrian Res. 79 (1–2), 3–24.
Coleman, M.L., 1993. Microbial processes: controls on the shape and composition of carbonate concretions. Mar. Geol. 113 (1–2), 127–140.
de Kock, M.O., Evans, D.A., Beukes, N.J., 2009. Validating the existence of Vaalbara in the Neoarchean. Precambrian Res. 174 (1–2), 145–154.
de Lange, G.J., Jarvis, I., Kuijpers, A., 1987. Geochemical characteristics and provenance of late Quaternary sediments from the Madeira Abyssal Plain, N Atlantic. Geol. Soc. (Lond.) Spec. Publ. 31 (1), 147–165.
de Oliveira Rodrigues, P.D.O.C., Hinnov, L.A., Franco, D.R., 2019. A new appraisal of depositional cyclicity in the Neoarchean-Paleoproterozoic Dales Gorge Member (Brockman Iron Formation, Hamersley Basin, Australia). Precambrian Res. 328, 27–47.
Frei, R., Gaucher, C., Poulton, S.W., Canfield, D.E., 2009. Fluctuations in Precambrian atmospheric oxygenation recorded by chromium isotopes. Nature 461 (7261), 250–253.
Gumsley, A.P., Chamberlain, K.R., Bleeker, W., Söderlund, U., de Kock, M.O., Larsson, E.R., Bekker, A., 2017. Timing and tempo of the Great Oxidation Event. Proc. Natl. Acad. Sci. USA 114 (8), 1811–1816.
Hancock, E.A., Green, A.A., Huntington, J.F., Schodlok, M.C., Whitbourn, L.B., 2013. HyLogger-3: Implications of Adding Thermal-Infrared Sensing. Geological Survey of Western Australia.
Haugaard, R., Pecoits, E., Lalonde, S., Rouxel, O., Konhauser, K., 2016. The Joffre banded iron formation, Hamersley Group, Western Australia: assessing the palaeoenvironment through detailed petrology and chemostratigraphy. Precambrian Res. 273, 12–37.

Hennekam, R., Sweere, T., Tjallingii, R., de Lange, G.J., Reichart, G.J., 2019. Trace metal analysis of sediment cores using a novel X-ray fluorescence core scanning method. Quat. Int. 514, 55–67.
Herbert, T.D., Fischer, A.G., 1986. Milankovitch climatic origin of mid-Cretaceous black shale rhythms in central Italy. Nature 321 (6072), 739–743.
Jones, C., Nomosatryo, S., Crowe, S.A., Bjerrum, C.J., Canfield, D.E., 2015. Iron oxides, divalent cations, silica, and the early earth phosphorus crisis. Geology 43 (2), 135–138.
Kasten, S., Zabel, M., Heuer, V., Hensen, C., 2003. Processes and signals of nonsteady-state diagenesis in deep-sea sediments and their pore waters. In: The South Atlantic in the Late Quaternary. Springer, Berlin, Heidelberg, pp. 431–459.
Kendall, B., Reinhard, C.T., Lyons, T.W., Kaufman, A.J., Poulton, S.W., Anbar, A.D., 2010. Pervasive oxygenation along late Archaean ocean margins. Nat. Geosci. 3 (9), 647–652.
Klein, C., Beukes, N.J., 1989. Geochemistry and sedimentology of a facies transition from limestone to iron-formation deposition in the early Proterozoic Transvaal Supergroup, South Africa. Econ. Geol. 84 (7), 1733–1774.
Koehler, M.C., Buick, R., Kipp, M.A., Stüeken, E.E., Zaloumis, J., 2018. Transient surface ocean oxygenation recorded in the ∼2.66-Ga Jeerinah Formation, Australia. Proc. Natl. Acad. Sci. USA 115 (30), 7711–7716.
Konhauser, K.O., Planavsky, N.J., Hardisty, D.S., Robbins, L.J., Warchola, T.J., Haugaard, R., Johnson, C.M., 2017. Iron formations: a global record of Neoarchaean to Palaeoproterozoic environmental history. Earth-Sci. Rev. 172, 140–177.
Krapež, B., Barley, M.E., Pickard, A.L., 2003. Hydrothermal and resedimented origins of the precursor sediments to banded iron formation: sedimentological evidence from the Early Palaeoproterozoic Brockman Supersequence of Western Australia. Sedimentology 50 (5), 979–1011.
Kutzbach, J.E., Xiaodong, L., Zhengyu, L., Guangshan, C., 2008. Simulation of the evolutionary response of global summer monsoons to orbital forcing over the past 280,000 years. Clim. Dyn. 30, 567–579.
Lalonde, S.V., Konhauser, K.O., 2015. Benthic perspective on Earth's oldest evidence for oxygenic photosynthesis. Proc. Natl. Acad. Sci. USA 112 (4), 995–1000.
Lantink, M.L., Davies, J.H., Mason, P.R., Schaltegger, U., Hilgen, F.J., 2019. Climate control on banded iron formations linked to orbital eccentricity. Nat. Geosci. 12 (5), 369–374.
Lantink, M.L., Davies, J.H., Ovtcharova, M., Hilgen, F.J., 2022. Milankovitch cycles in banded iron formations constrain the Earth–moon system 2.46 billion years ago. Proc. Natl. Acad. Sci. USA 119 (40), e2117146119.
Lenstra, W.K., Egger, M., Van Helmond, N.A., Kritzberg, E., Conley, D.J., Slomp, C.P., 2018. Large variations in iron input to an oligotrophic Baltic Sea estuary: impact on sedimentary phosphorus burial. Biogeosciences 15 (22), 6979–6996.
Lyons, T.W., Reinhard, C.T., Planavsky, N.J., 2014. The rise of oxygen in Earth's early ocean and atmosphere. Nature 506 (7488), 307–315.
Martin, D.M., Clendenin, C.W., Krapez, B., McNaughton, N.J., 1998. Tectonic and geochronological constraints on late Archaean and Palaeoproterozoic stratigraphic correlation within and between the Kaapvaal and Pilbara Cratons. J. Geol. Soc. 155 (2), 311–322.
Meyers, S.R., 2012. Seeing red in cyclic stratigraphy: spectral noise estimation for astrochronology. Paleoceanography 27 (3).
Meyers, S.R., 2014. Astrochron: an R package for astrochronology. https://cran.rproject.org/web/packages/astrochron/index.html.
Meyers, S.R., Sageman, B.B., Arthur, M.A., 2012. Obliquity forcing of organic matter accumulation during Oceanic Anoxic Event 2. Paleoceanography 27 (3).
Middelburg, J.J., Soetaert, K., Hagens, M., 2020. Ocean alkalinity, buffering and biogeochemical processes. Rev. Geophys. 58 (3), e2019RG000681.
Mitchell, R.N., Bice, D.M., Montanari, A., Cleaveland, L.C., Christianson, K.T., Coccioni, R., Hinnov, L.A., 2008. Oceanic anoxic cycles? Orbital prelude to the Bonarelli Level (OAE 2). Earth Planet. Sci. Lett. 267 (1–2), 1–16.
Morris, R.C., Horwitz, R.C., 1983. The origin of the iron-formation-rich Hamersley Group of Western Australia—deposition on a platform. Precambrian Res. 21 (3–4), 273–297.
Ostrander, C.M., Nielsen, S.G., Owens, J.D., Kendall, B., Gordon, G.W., Romaniello, S.J., Anbar, A.D., 2019. Fully oxygenated water columns over continental shelves before the Great Oxidation Event. Nat. Geosci. 12 (3), 186–191.
Passier, H.F., Middelburg, J.J., van Os, B.J., de Lange, G.J., 1996. Diagenetic pyritisation under eastern Mediterranean sapropels caused by downward sulphide diffusion. Geochim. Cosmochim. Acta 60 (5), 751–763.
Pickard, A.L., Barley, M.E., Krapež, B., 2004. Deep-marine depositional setting of banded iron formation: sedimentological evidence from interbedded clastic sedimentary rocks in the early Palaeoproterozoic Dales Gorge Member of Western Australia. Sediment. Geol. 170 (1–2), 37–62.
Potts, P.J., Williams-Thorpe, O., Webb, P.C., 1997. The bulk analysis of silicate rocks by portable X-ray fluorescence: effect of sample mineralogy in relation to the size of the excited volume. Geostand. Newsl. 21 (1), 29–41.
Poulton, S.W., Canfield, D.E., 2011. Ferruginous conditions: a dominant feature of the ocean through Earth's history. Elements 7 (2), 107–112.
Poulton, S.W., Bekker, A., Cumming, V.M., Zerkle, A.L., Canfield, D.E., Johnston, D.T., 2021. A 200-million-year delay in permanent atmospheric oxygenation. Nature 592 (7853), 232–236.
Reichart, G.J., Lourens, L.J., Zachariasse, W.J., 1998. Temporal variability in the northern Arabian Sea oxygen minimum zone (OMZ) during the last 225,000 years. Paleoceanography 13 (6), 607–621.
Reinhard, C.T., Planavsky, N.J., 2020. Biogeochemical controls on the redox evolution of Earth's oceans and atmosphere. Elements 16 (3), 191–196.
Reinhard, C.T., Planavsky, N.J., Olson, S.L., Lyons, T.W., Erwin, D.H., 2016. Earth's oxygen cycle and the evolution of animal life. Proc. Natl. Acad. Sci. USA 113 (32), 8933–8938.
Röhling, E.J., Marino, G., Grant, K.M., 2015. Mediterranean climate and oceanography, and the periodic development of anoxic events (sapropels). Earth-Sci. Rev. 143, 62–97.
Rossignol-Strick, M., 1983. African monsoons, an immediate climate response to orbital insolation. Nature 304 (5921), 46–49.
Simonson, B.M., Hassler, S.W., 1996. Was the deposition of large Precambrian iron formations linked to major marine transgressions? J. Geol. 104 (6), 665–676.
Sumner, D.Y., Grotzinger, J.P., 1996. Were kinetics of Archean calcium carbonate precipitation related to oxygen concentration? Geology 24 (2), 119–122.
Thomson, D.J., 1982. Spectrum estimation and harmonic analysis. Proc. IEEE 70 (9), 1055–1096.
Trendall, A.F., 1969. The Joffre Member in the Gorges South of Wittenoom. In: Geological Survey of Western Australia Annual Report 1968.
Trendall, A.F., 1972. Revolution in earth history: Presidential address delivered in Brisbane on 25 May 1971. J. Geol. Soc. Aust. 19 (3), 287–311.
Trendall, A.F., 2002. The significance of iron-formation in the Precambrian stratigraphic record. In: Precambrian Sedimentary Environments: A Modern Approach to Ancient Depositional Systems, pp. 33–66.
Trendall, A.F., Blockley, J.B., 1970. The Iron Formations of the Precambrian Hamersley Group Western Australia with Special Reference to the Associated Crocidolite. Geological Survey of Western Australia.
Tyrrel, T., 1999. The relative influences of nitrogen and phosphorus on oceanic primary production. Nature 400, 525–531.
van de Velde, S.J., Reinhard, C.T., Ridgwell, A., Meysman, F.J., 2020. Bistability in the redox chemistry of sediments and oceans. Proc. Natl. Acad. Sci. USA 117 (52), 33043–33050.
van Hoof, A.A.M., Van Os, B.J.H., Rademakers, J.G., Langereis, C.G., De Lange, G.J., 1993. A paleomagnetic and geochemical record of the upper Cochiti reversal and two subsequent precessional cycles from southern Sicily (Italy). Earth Planet. Sci. Lett. 117 (1–2), 235–250.
van Os, B.J.H., Lourens, L.J., Hilgen, F.J., De Lange, G.J., Beaufort, L., 1994. The formation of Pliocene sapropels and carbonate cycles in the Mediterranean: diagenesis, dilution, and productivity. Paleoceanography 9 (4), 601–617.
Waltham, D., 2015. Milankovitch period uncertainties and their impact on cyclostratigraphy. J. Sediment. Res. 85 (8), 990–998.
Wang, Y., Van Cappellen, P., 1996. A multicomponent reactive transport model of early diagenesis: application to redox cycling in coastal marine sediments. Geochim. Cosmochim. Acta 60 (16), 2993–3014.
Warke, M.R., Di Rocco, T., Zerkle, A.L., Lepland, A., Prave, A.R., Martin, A.P., Claire, M.W., 2020. The great oxidation event preceded a paleoproterozoic "snowball Earth". Proc. Natl. Acad. Sci. USA 117 (24), 13314–13320.
Weltje, G.J., Bloemsma, M.R., Tjallingii, R., Heslop, D., Röhl, U., Croudace, I.W., 2015. Prediction of geochemical composition from XRF core scanner data: a new multivariate approach including automatic selection of calibration samples and quantification of uncertainties. In: Micro-XRF Studies of Sediment Cores. Springer, Dordrecht, pp. 507–534.
Wogan, N.F., Catling, D.C., Zahnle, K.J., Claire, M.W., 2022. Rapid timescale for an oxic transition during the Great Oxidation Event and the instability of low atmospheric O_2. Proc. Natl. Acad. Sci. 119 (37), e2205618119.